SAND2017-2520J

Riverbed Hydrologic Exchange Dynamics in a Large Regulated River Reach

Zhou T.[1], J. Bao[1], M. Huang[1], Z. Hou[1], E. Arntzen[1], R. Mackley[1], S. Harding[1], S. Titzler[1], C. Murray[1], W. Perkins[1], X. Chen[1], J. Stegen[1], G. Hammond[2], P. Thorne[1], J. Zachara[1]

1. Pacific Northwest National Laboratory, Richland, WA, USA
2. Sandia National Laboratories, Albuquerque, NM, USA

To be submitted to *Water Resources Research*

Abstract

Hyporheic exchange is an important mechanism taking place in riverbanks and riverbed sediments, where river water and shallow groundwater mix and interact with each other. The direction, magnitude, and residence time of the hyporheic flux that penetrates the river bed are critical for biogeochemical processes such as carbon and nitrogen cycling, and biodegradation of organic contaminants. Many approaches including field measurements and numerical methods have been developed to quantify the hyporheic exchanges in relatively small rivers. However, the spatial and temporal distributions of hyporheic exchanges in a large, regulated river reach remain less explored due to the large spatial domains, complexity of geomorphologic features and subsurface properties, and the great pressure gradient variations at the riverbed created by dam operations.

In this study, we developed a method that combined numerical modeling and field measurements for estimating hyporheic fluxes across the river bed in a 7-km long reach of the highly regulated Columbia River. The reach has a minimum width of about 800 meters and variations in river stage within a day could be up to two meters due to the upstream dam operations. A high-resolution computational fluid dynamics (CFD) modeling framework was developed and validated by the field measurements and other modeling results to characterize the spatial distribution of flux rates across the river bed at different river flow conditions. An empirical relationship was then established between the reach-scale hyporheic flux rates and the flow conditions in order to examine the hyporheic dynamics at any given flow conditions. We found that the mean hyporheic exchange rate is about -0.6 $m^3 s^{-1}$ across the entire river reach from 2008 to 2014 with temporal variability at multiple scales. This approach is general and extendable to other natural and managed river reaches for quantifying hyporheic exchange dynamics by relating the estimated fluxes with river discharge through

simple relations, and combining with geomorphological and hydrogeological characterizations of river reaches for watershed scale applications

1. Introduction

The hyporheic zone is a critical component in the fluvial system, located in the aquifer surrounding the river channel [*Harvey et al.*, 1996; *Gooseff*, 2010]. Surface water transfers through the hyporheic zone and mixes with groundwater via intrusion and then returns to the river, making the hyporheic zone a critical spot for biogeochemical processes such as carbon and nitrogen cycling, and biodegradation of organic contaminants [*Findlay et al.*, 1993; *Valett et al.*, 1996; *Sobczak and Findlay*, 2002; *Anderson et al.*, 2005; *Zarnetske et al.*, 2011a, 2011b]. Hyporheic exchange dynamics, including the direction and magnitude of the hyporheic flux as well as the retention time of flow in the hyporheic zone define where and when the biogeochemical processes occur and residence time of species in the hyporheic zone [*Morrice et al.*, 1997; *Boulton et al.*, 1998; *Tonina and Buffington*, 2007]. Hyporheic flows are controlled by channel geometry, basin geology, and hydrology [*Brunke et al.*, 1997; *Winter*, 1999], but essentially the governing factors of the hyporheic flux rate are permeability and hydraulic gradients in the porous media. In a highly regulated river, the hydraulic gradient not only reflects the hydrometeorological characteristics in the catchment, more importantly, it is determined by the river stage variations from upstream dam operations. The impacts of dam operations on river flow and hydraulics could extend to a few hundred kilometers downstream of a dam [*Arntzen et al.*, 2006] with a wide spectrum of timescales from hourly to monthly [*Poff et al.*, 1997].

Hyporheic exchanges in regulated river systems have been studied via field measurements or modeling tools in previous studies at the point [e.g. *Arntzen et al.*, 2006] or transect scales [e.g. *Sawyer et al.*, 2009; *Cardenas and Markowski*, 2011; *Gerecht et al.*, 2011]. These fine-scale studies usually employed Darcy's Law or heat transport equations by monitoring head differences or temperature time series at different depths [*Kalbus et al.*, 2006]. They are important and necessary for understanding the

fundamental physical and biological processes in the hyporheic zone [*Harvey and Gooseff*, 2015]. These point measurements can be further interpolated to a 2D or 3D domain to characterize the hyporheic exchange dynamics in both space and time at reach scales [e.g. *Gerecht et al.*, 2011; *Anibas et al.*, 2015]. They could also be combined with statistical methods to quantify hyporheic dynamics. For example, *Conant* [2004] established an empirical relationship between simultaneously obtained flux data from mini-piezometers and riverbed temperature in a 60-meter long river section. This method allows researchers to generate a spatial distribution of hyporheic fluxes by simply sampling temperatures over the river bed in relatively small river systems. However, the point measurement-based approaches are often subjected to a great level of uncertainties due to simplified assumptions and instrument accuracy. Most of them are not suited for large-scale studies because of the intensive data requirement over large spatial and temporal domains, especially in our study river reach (explained in next section) which has a width of nearly 1000 m and a depth of over 10 m along the thalweg. Therefore, using numerical modeling to estimate the hyporheic flux became popular in the past few decades because of its flexibility on domain configurations and reduction in measurement and computational expenses. Numerical modeling has been proven in many studies as a robust tool for quantifying flow dynamics and for understanding fundamental physical and biogeochemical processes in the hyporheic zone [e.g. *Cardenas et al.*, 2004; *Lautz and Siegel*, 2006; *Tonina and Buffington*, 2007; *Stonedahl et al.*, 2010; *Janssen et al.*, 2012; *Trauth et al.*, 2013; *Zhou and Endreny*, 2013]. However, applying a coupled surface water – groundwater model in a large river reach remains less explored.

Hyporheic exchanges in rivers occur at various scales ranging from a single point or transect to a basin. Yet, most of the previous studies mentioned above focused on small-scale applications. The increasing needs of linking small-scale hyporheic physical

100 and biogeochemical processes to larger scale integrated behaviors have attracted
101 attention from the community in recent years [*Harvey and Gooseff*, 2015]. *Kiel and*
102 *Cardenas* [2014] estimated lateral hyporheic exchanges in three large river basins
103 (Missouri, Upper Mississippi, and Ohio) using a simple relation at the river reach scale
104 that connects lateral hyporheic fluxes to river discharge and local channel geomorphic
105 features such as channel width, depth, sinuosity, and valley slope. *Gomez-Velez et al.*
106 [2015] attempted to compare the relative importance of hyporheic exchange through
107 sedimentary structures on the river bottom and lateral transfer using a physically based
108 hyporheic flow model along the river network of the Mississippi River Basin. These
109 applications demonstrate the feasibility of establishing linkages across scales in
110 hyporheic studies. However, these studies were limited to steady flow conditions,
111 therefore their approaches aren't very applicable to the study of regulated rivers with
112 highly dynamic flow rates.

113 In this study, we aim to quantify the hyporheic exchange based on numerical
114 simulations and link the reach-scale exchange with the river discharge and inland water
115 table level in a large, dam-regulated river reach. Such a linkage is crucial for
116 parameterizing reach-scale hyporheic exchange rates from small-scale mechanistic
117 models to applications at larger scales in both space and time, such as the one by *Kiel*
118 *and Cardenas* [2014]. In our modeling framework, a loosely coupled computational fluid
119 dynamics (CFD) model was established and validated against surface flow hydraulics
120 data and fluxes estimated based on field temperature measurements. The CFD model
121 was then applied over the selected river reach under various flow conditions and inland
122 water level configurations to investigate the relation between net hyporheic exchanges
123 at the reach scale in response to various flow conditions.

124 To summarize, the goals of this study are 1) to quantify the averaged hyporheic
125 exchange rates over a large river reach with highly variable flows caused by dam-

126 regulation using a CFD model; and 2) to examine how the reach-scale hyporheic
127 exchange is driven by the highly dynamic river stage versus the more stable inland
128 water table conditions; and use the established relation to reconstruct historical
129 hyporheic dynamics in the study reach. In section 2, we describe the study domain and
130 CFD model validations. In section 3, we analyze the results, and then discuss the
131 uncertainties of the methods and conclude in section 4.

132 # 2. Method

133 ### *2.1 Study reach*

134 Our study reach is a 7-km long, 800-meter wide, nearly straight river segment
135 inside the U.S. Department of Energy Hanford Site, near the 300A area (**Figure 1**). The
136 Columbia River flows from north to south through the study reach over a 40 - 60 m
137 thick aquifer, which consists of two major hydrogeological units: a highly permeable
138 Pleistocene flood gravel layer of the Hanford Formation on top and a more consolidated
139 and less permeable Miocene to Pliocene fluvial deposition layer of the Ringold
140 Formation at the bottom. At the very top of the river bed, there is a thin layer of
141 alluvium with varying thicknesses ranging from one to three meters [*Hartman and*
142 *Dresel*, 1998]. Along the river there are a number of sandbar islands, forming a deep
143 primary channel and a relatively shallower secondary channel on the opposite side of
144 the islands (**Figure 1**). A hydroelectric dam (Priest Rapids Dam) is located about 80 km
145 upstream of the study reach. According to the historical river stage record at the study
146 reach during the past 40 years, the stage levels could vary two meters in maximum
147 within a day with a range between 105 m to 109 m based on the North American
148 Vertical Datum of 1988 (NAD88). In this study, the river stage observations were
149 recorded every 30 mins by a pressure transducer logger (SWS-1) installed inside our
150 study domain since the year 2001. A monitoring well (Well 2-3), about 150m from the
151 river, was used as the reference point of the inland water level (**Figure 1**).

2.2 Modeling strategy

The surface water hydrodynamics and hyporheic flows were simulated in a CFD model for the study river reach (**Figure 2**). In the following sub-sections, model configurations, inputs, and validations will be explained in details.

2.2.1 High resolution CFD model

The centerpiece of our modeling framework is a high resolution CFD model that seamlessly couples surface and subsurface flow simulations in a two-region mesh setup using the commercial code STAR-CCM® (CD-adapco, 2015). The modeling domain is divided into surface flow and subsurface flow regions with a shared river bed surface. The simulation was first spun up in the surface flow region to reach the equilibrium and then the established pressure field at the riverbed was applied as the upper boundary condition for the subsurface domain. The CFD model solves the mass and momentum conservation equations for surface fluid dynamics using the finite volume method with turbulences represented by k-ε two-layer model and the fluid-air interface captured by the Volume of Fluid (VOF) approach. In the subsurface domain, a large viscous resistance term was applied to the flow in order to mimic the resistance induced by the porous media. The viscous porous resistance tensor is determined by the horizontal and vertical permeability of the sediment. The equations of the CFD model are described in the supplementary materials (**S.1**).

We used unstructured prism meshes for both domains. The horizontal resolution of the mesh ranges from 1 m to 25 m, and is finer close to the river-sediment interface and near the river banks and coarser toward the center of channels. To better capture the dynamic vertical exchange, the vertical resolution of the mesh was set to 0.25 m to 0.45 m and denser near the riverbed. The total number of grid cells is ~6,500,000 for the surface water domain and ~8,600,000 for the subsurface domain. The channel geometry in the CFD model was configured based on the riverbed bathymetry derived from a 1-

178 m resolution LiDAR river bathymetry dataset taken in the year of 2008 [*Coleman et al.*,
179 2010]. We simplified the subsurface domain as three geological layers overlapping with
180 each other horizontally (from top to bottom: Hanford, Ringold Gravel, Ringold Lower
181 Mud) and a 2-m thick fourth layer on top of the riverbed to represent the alluvium layer
182 (**Figure 3**). The porosity and permeability of the three horizontal layers were estimated
183 based on the well data collected previously in the 300 Area [*Hartman and Dresel*, 1998]
184 (**Table 1**). Given that the alluvium layer was formed by the sediment depositions, the
185 permeability, which is essentially governed by the grain sizes of the sediments and
186 strongly affects the hyporheic flux rate, is highly dependent on the local stream power
187 (i.e. flow speed and slope). Thus a great heterogeneity of the alluvium layer
188 permeability is expected over the river bed. In this study, the spatial distribution of the
189 alluvium layer permeability was extrapolated from an underwater video-camera
190 footage based grain-size analysis [*Fritz et al.*, 2007]. In this analysis, underwater video
191 footage of the riverbed was collected along numerous transects across the study reach.
192 The grain size of the largest sediment was measured in each footage, with the sizes
193 ranging from sand to boulder. We used the Kozeny–Carman equation (**Eq 1**) to estimate
194 the permeability of the alluvium layer based on the grain size of the bedload sediment:

195 $$K = \frac{D^2 \emptyset^2 n^2}{180 \rho g (1-n)^2} \quad (1)$$

196 where K is the permeability, D is the median grain size of the sediment, $\emptyset$ is the
197 sphericity of the particles in the river bed, n is the porosity, ρ is the density of water, g is
198 the gravitational acceleration. Given that only the largest bedload sediment was
199 measured in the video footage, we normalized these grain size measurements to the
200 range between the Hanford and Ringold sediment (**Figure 4**) as these layers might be
201 the major sediment sources of the alluvium layer. We assumed the sphericity was 0.7
202 and porosity was 0.2.

The boundary conditions that drove the CFD model were generated based on model estimates and field measurements. For the surface flow simulation, the river stage and velocity at upstream and downstream boundaries were directly taken from a well-established 1-D hydraulic model (Modular Aquatic Simulation System in 1-Dimension or MASS1). The MASS1 model was originally developed for simulating hydrodynamics in the Hanford Reach of the Columbia River [*Richmond and Perkins*, 2002; *Richmond and Perkins*, 2009; *Niehus et al.*, 2014]. It simulates transient flow in rivers and canals by solving the one-dimensional, cross-section averaged equations of mass and momentum conservations (St. Venant equations). The simulation results have been applied to a variety of problems in the Columbia River basin with relatively high accuracy in predicting flow stage profiles along the Hanford Reach (MAE less than 0.15m and bias less than 0.06 m against field measurements at hourly basis during validation periods) (e.g. *McMichael et al.*, 2005; *Tiffan et al.*, 2002). Calibration and validation details of MASS1 model can be found in the supplementary materials (**S.2**). In this study, flow conditions were simulated at hourly basis in MASS1 from 1 January 1976 to 19 February 2016 for the Hanford Reach from the Priest Rapids Dam to the 300 Area (about 80 km). The MASS1-simulated river stage, discharge, and averaged flow velocity were exported at a series of cross-sections along the river with an interval of ~200 m. The two cross-sections that are close to the CFD upstream and downstream boundaries were selected to provide CFD boundary conditions for the historical simulations. For the simulation period that the MASS1 simulation is not available (i.e. after 19 February 2016), the river stage data was first taken from SWS-1 river gauge observations and then translated to river discharge data via a long term (over 40 years) rating curve generated from MASS1 at the SWS-1 cross-section. CFD boundary conditions were then derived from the estimated discharge based on MASS1 rating curves at upstream and downstream cross-sections. The inland water table level was

229 based on the Well 2-3 recorded data, with a consistent water table gradient (1.2×10^{-4})
230 averaged from historical well monitoring data [*Williams et al.*, 2008].

231 *2.2.2 CFD model validation*

232 We validated the CFD model for both surface and subsurface domains. The CFD
233 simulated hyporheic flow was driven by the pressure gradients across the river bed.
234 Therefore an accurate pressure boundary at the surface-water and groundwater
235 interface is a prerequisite for modeling the hyporheic flux. Given that the pressure on
236 the river bed is essentially a combination of river stage and pressure from the near-bed
237 surface flow velocity, we validated the flow velocity profiles and flow surface elevation
238 against the Acoustic Doppler Current Profiler (ADCP) measurements and MASS1
239 simulated results. The ADCP measurements were carried out at four transects over the
240 study reach (A, B, C, and D in **Figure 1**) on 19 February 2016 from 12 pm to 4 pm. These
241 transects were selected to cover the entire channel width (transect C), main channel
242 with deep bathymetry and relatively high flow velocity (transects A and D), and
243 secondary channel with shallow bathymetry and lower flow velocity (transect B). A
244 vessel mounted 1200 kHz RDI Workhorse Sentinel ADCP was used to measure the flow
245 velocity profiles with 0.5 m vertical interval and 0.2 Hz output frequency.
246 Measurements at each transact were repeated twice and the total discharge were
247 consistent within 10% error range. The CFD model was driven by boundary conditions
248 from the MASS1 model on the same day at 2pm PST. The CFD simulated streamwise
249 velocity (v_y) vs. depth profiles at 1/6, 1/3, 1/2, 2/3, and 5/6 width of the four cross
250 sections were compared with ADCP measurements, and overlaid on the spatial
251 distributions of the percentage difference between ADCP measurements and CFD
252 predictions over the transect-averaged ADCP streamwise velocity (**Figure 5**). The
253 comparisons suggested that the CFD simulation results captured the velocity profiles
254 and patterns reasonably well with over 80% of the area having differences less than 20%

255 of the mean velocity. In some cases such as the cross-sections C and D, noticeable
256 deviations can be observed near the bed. This may be due to the uncertainties of the
257 ADCP measurements, the spatial resolution of the CFD model and the geometry used
258 in the CFD model. In addition, the river stage raised about 0.2 m during the measuring
259 period, which may also lead to the deviations between the measurements and the
260 simulation results.

261 CFD simulated river surface elevations along the study reach were compared
262 with the MASS1 simulated stage every 200 m along the study reach (**Figure 6**). In each
263 segment, the CFD simulated stage were extracted from every node within the segment
264 and presented as box plots against the MASS1 simulations. The comparisons showed
265 that the CFD model adequately captured the general gradient of the flow surface.
266 Greater stage variations were observed in the CFD simulations because MASS1 is a 1-D
267 model which cannot predict the wave heights and the stage differences from two sides
268 of the islands. The validation results of flow velocity profiles and river stage suggested
269 that pressure heads assigned to the subsurface domain in the CFD model captured the
270 spatial distribution and magnitude of the reality.

271 Next, the CFD simulated hyporheic fluxes were validated with temperature
272 based flux estimates. We quantified point hyporheic exchanges by combining
273 temperature measurements and inland water table and flow conditions. The
274 temperature data was measured by sensors (iButton® DS1922L) at five locations along
275 the west bank of the river (see **Figure 1**). The monitoring locations were selected based
276 on the local hydrodynamic conditions and river bed properties. From north to south,
277 sites A and B are located in the secondary channel with relatively low flow velocities
278 and small sediment sizes on the river bed, while sites D and E are located in the
279 primary channel with relatively high flow velocities and large grain sizes in riverbed.
280 Site C is in the transient zone between sites B and D. All sensors were programmed to

record every 10 minutes from 2 March to 30 March 2016. The vertical hyporheic fluxes at these monitoring sites were estimated using a method that combines a Maximum Likelihood estimator (LPML) developed by *Vandersteen et al.* [2015], a 1-D heat transfer model described in *Turcotte and Schubert* [1982], and a regression relationship between flow conditions and hyporheic fluxes [see *Zhou et al.* 2017 for details]. Three flow conditions from the iButton monitoring period were selected as the validation scenarios, representing the high flow (i.e., March 10th), median flow (i.e., March 28th), and low flow (i.e., March 8th) conditions, respectively (**Figure 7A**). The CFD simulated vertical flux rates across the river bed were exported from the three simulation scenarios (**Figure 7B**) and compared with iButton estimated flux ranges (**Figure 7C**). The comparisons suggest that most of the hyporheic fluxe rates at the five iButton sites were predicted within the ranges indicated by the ibutton-based estimates, and the CFD model adequately captures the differences between primary and secondary channels in terms of magnitudes of fluxes. Due to limitations such as accessibility, we were unable to validate the hyporheic flux rate in deep water by measurements. However, the CFD simulated spatial patterns of vertical fluxes over the riverbed (**Figure 7B**) did agree with field observations [e.g. *Gerecht et al.*, 2011] and numerical modeling results [e.g. *Boano et al.*, 2008] from other studies, featuring strong exchanges near the bank and weak exchanges at the center of the channel due to head gradient differences.

2.2.3 CFD modeling setups

The validated CFD model was then used to investigate the reach-scale hyporhic exchange under different flow conditions. A historical period from 1 January 2008 to 31 December 2014 was selected to provide representitive CFD modeling flow conditions, during which the Well 2-3 data and MASS1 output both are availabe and continuous. We randomly selected 50 daily flow conditions for the surface flow and the inland water table level to drive the CFD model. These flow condition samples were

representitive of this period as they have similar empirical distribution functions to those based on data from the entire period (**Figure 8**). We assume that the reach-scale hyporheic exchange rate is highly related to the river discharge (stage) and the inland water table level. Therefore a response surface analysis was conducted based on the 50 simulation cases to quantify the historical hyporheic exchanges.

3. Results

The 50 simulation results were analyzed at the reach scale. For each case, we aggregated the vertical fluxes at the riverbed over the study domain but discarded those within the first and last 200 meters of the domain to avoid numerical uncertainties near boundaries. By doing so, the net hyporheic exchange for the entire river segment is calculated and denoted as reach-scale hyporheic exchange rate (Q_Z). The rates range from -3.33 $m^3 s^{-1}$ to 1.55 $m^3 s^{-1}$ over the 50 cases. **Figure 9** shows the spatial distributions of vertical fluxes of the modeling domain at the lowest and highest river discharge (Q_R) (**Figure 9 A, B**) and at the strongest hyporheic zone discharging (maximum Q_Z) and strongest recharging (minimum Q_Z) conditions (**Figure 9 C, D**). The results revealed that stronger hyporheic exchanges always occurred along the shoreline in shallow water area, with magnitudes of the fluxes ranging between $\pm 5\times10^{-6}$ m s^{-1}. The results also suggest that low flow (**Figure 9 A, C**) and high flow conditions (**Figure 9 B, D**) are usually associated with discharging and recharging conditions in the hyporheic zone, respectively. However, the river discharge is not monotonically related to the reach-scale hyporheic exchange. That is, the highest river discharge does not imply the strongest recharging condition and vice versa. Previous studies at the point scale in our study reach [*Fritz and Arntzen*, 2007; *Zhou et al.*, 2017] suggest that the point-scale hyporheic exchange flux was linearly related to the head difference between the river stage and the inland water table level, indicating that the inland water table elevation (h) is another major factor that controls the reach-scale hyporheic flux (Q_Z). Here we

empirically related the Q_Z to the Q_R and h by constructing a response surface using a 1st order polynomial function (**Eq 2**) with a R^2 of 0.8 (**Figure 10**).

$$Q_z = -0.002356Q_R + 4.998h - 519.5 \quad (2)$$

Based on this response surface, values of Q_Z for the study domain over a seven-year period (i.e., from January 2008 to December 2014) were estimated based on water level measurements from Well 2-3 and river discharge data from the MASS1 model (**Figure 11**). The results suggested that about 70% of the time the hyporheic zone in our study domain is under recharging conditions from the river to subsurface with a median Q_z of ~-0.6 $m^3 s^{-1}$ or ~0.02% of the median river discharge. By analyzing the seasonality of the time series, we find that the hyporheic zone discharge always occurs in the early fall (e.g. September) with a mean Q_z of about 0.1 $m^3 s^{-1}$. This might be caused by the rapid dropping in river stage during this period.

4. Discussion and conclusion

In this study, we introduced an approach to infer reach-scale hyporheic exchange rates based on numerical simulations combining with the stage-flux relationship. The strength of this approach is that it considers short-term river stage variations imposed by flow regulations (i.e., dam operations). Such short-term variations rarely occur in a natural river except for during a big flooding event. This assumption was supported by the field data at our study site [*Zhou et al.* 2017] manifested as prompt head variations created by river stage fluctuations as a results of releases from the upstream hydroelectric dam. However, it may not be generally applicable to other fluvial systems if there is a confined aquifer with its pressure driven by more distant locations such as natural rivers with constant groundwater discharge. In small highland rivers, local geomorphological features such as riffles and pools might be a greater dominant factor

than the head difference in controlling hyporheic exchange rates [*Crispell and Endreny*, 2009; *Byrne et al.*, 2014].

A coupled CFD model was employed to simulate hyporheic exchange dynamics under various flow conditions. Although the CFD model was parameterized and forced by field measurements and observations, it is subject to uncertainties rooted from the following sources: 1) uncertainty about the thickness of geological units. For this study, we simplified these units as horizontal layers with constant thicknesses across the domain. However variations of the boundary between the highly permeable Hanford layer and Ringold layer with a low permeability could be up to 4 m along the shoreline of the 300A area, therefore could significantly affect local hyporheic flow directions and magnitudes [*Slater et al.*, 2010]. 2) the physical properties of the geological units, such as sediment permeability and grain sizes. The values currently used in the CFD model are either from literature or from point measurements in the riverbed (e.g., by extracting freeze cores *[Hou et al., 2016]*), therefore does not represent the heterogeneity over the whole domain. 3) the bathymetry data and the associated meshing in the CFD model. The bathymetry data were taken in 2008 and used to validate surface flow hydrodynamics measured in 2016. Although the segment of the Columbia River in the study domain is relatively stable, the geometry of the channel still gradually changed over time. For example, a land slide occurred in 2015 reshaped the east bank of the channel about 2km downstream of the northern boundary of our study reach. There are also uncertainties associated with the boundary conditions to the CFD model, such as the simulations from the MASS 1 hydrodynamic model.

By examining the spatial distribution of vertical fluxes at the riverbed over the study domain, we found that the direction of hyporheic fluxes at some areas (e.g. the fluxes are always positive in some areas between the two major islands) regardless the direction of Q_Z. This indicates that even in large regulated rivers, some hyporheic fluxes

may still be dominated by the local geomorphological features [*Cardenas et al.*, 2004]. The hyporheic flow is controlled by hydrostatic and hydrodynamic drivers. The hydrostatic driver is determined by the flow height and tends to be more influential beneath the larger, emergent topographic features; while the hydrodynamic driver is determined by local flow velocity fields and tends to drive shallow hyporheic flows through pathways that are typically shallower than the stream depth [*Boano et al.*, 2014]. This also suggests that the consistent hyporheic fluxes near the islands may not go too deep into the sediment.

Based on the CFD simulations for the 50 scenarios we established an empirical relationship for reach-scale hyporheic exchange estimations. This simple method allows us to extend the study domain from a single segment of the river to the whole watershed when taking into account water table information from large-scale groundwater models such as from MODFLOW applications (e.g. over the Yakima Basin by *Ely et al*. [2011]). One limitation of this study is that we treat the segment as a straight channel and only vertical flux was calculated. In a meandering river, a combination with lateral flux estimation is necessary when accounting for fluvial geomorphic features such as valley slope and channel sinuosity [*Cardenas*, 2009]. In addition, the depth of the permeable layer is an important factor that may control the magnitudes of vertical and lateral hyporheic fluxes, which also needs to be taken into account in large scale surface water - groundwater interaction studies.

To summarize, in this study, a coupled CFD model, validated by the field observations and other modeling results, was employed to simulate the reach-scale hyporheic dynamics. Our estimates suggest that from 2008 to 2014 about 70% of the time the hyporheic zone in the study domain was under recharging conditions with the median hyporheic discharge of about -0.6 $m^3 s^{-1}$. This approach is general and extendable to other natural and managed river reaches for quantifying hyporheic

409 exchange dynamics as well as the residence time of water and solute in the hyporheic
410 zone. It helps developing parameterizations of hyporheic exchanges in larger scale
411 models by relating the estimated fluxes with river discharge through simple relations,
412 such as the simple response surface constructed in this studies, and combining with
413 geomorphological and hydrogeological characterizations of river reaches for watershed
414 scale applications [e.g. *Gomez-velez and Harvey*, 2014].

Acknowledgement

This research was supported by the U.S. Department of Energy (DOE), Office of Biological and Environmental Research (BER), as part of BER's Subsurface Biogeochemistry Research Program (SBR). This contribution originates from the SBR Scientific Focus Area (SFA) at the Pacific Northwest National Laboratory (PNNL). We thank Ms. Sara Niehus for her technical support on the MASS1 simulations.

References

Anderson, J. K., S. M. Wondzell, M. N. Gooseff, and R. Haggerty (2005), Patterns in stream longitudinal profiles and implications for hyporheic exchange flow at the H.J. Andrews Experimental Forest, Oregon, USA, *Hydrol. Process.*, *19*(15), 2931–2949, doi:10.1002/hyp.5791.

Anibas, C., U. Schneidewind, G. Vandersteen, I. Joris, P. Seuntjens, and O. Batelaan (2015), From streambed temperature measurements to spatial-temporal flux quantification: using the LPML method to study groundwater-surface water interaction, *Hydrol. Process.*, *216*(November), n/a-n/a, doi:10.1002/hyp.10588.

Arntzen, E. V., D. R. Geist, and P. E. Dresel (2006), Effects of fluctuating river flow on groundwater/surface water mixing in the hyporheic zone of a regulated, large cobble bed river, *River Res. Appl.*, *22*(8), 937–946, doi:10.1002/rra.947.

Boano, F., R. Revelli, and L. Ridolfi (2008), Reduction of the hyporheic zone volume due to the stream-aquifer interaction, *Geophys. Res. Lett.*, *35*(9), 1–5, doi:10.1029/2008GL033554.

Boano, F., J. W. Harvey, A. Marion, A. I. Packman, R. Revelli, L. Ridolfi, and A. Wörman (2014), Hyporheic flow and transport processes: Mechanisms, models, and bioghemical implications, *Rev. Geophys.*, 1–77, doi:10.1002/2012RG000417.Received.

Boulton, A., S. Findlay, and P. Marmonier (1998), The functional significance of the hyporheic zone in streams and rivers, *Annu. Rev. Ecol. Syst.*, *29*(1998), 59–81, doi:10.1146/annurev.ecolsys.29.1.59.

Brunke, M., T. Gonser, M. Brunke, T. Gonser, and T. Gonser (1997), The ecological significance of exchange processes between rivers and groundwater, *Freshw. Biol.*, *37*, 1–33, doi:10.1046/j.1365-2427.1997.00143.x.

445 Byrne, P., A. Binley, A. L. Heathwaite, S. Ullah, C. M. Heppell, K. Lansdown, H. Zhang,
446 M. Trimmer, and P. Keenan (2014), Control of river stage on the reactive chemistry
447 of the hyporheic zone, *Hydrol. Process.*, *28*(17), 4766–4779, doi:10.1002/hyp.9981.

448 Cardenas, M. B. (2009), A model for lateral hyporheic flow based on valley slope and
449 channel sinuosity, *Water Resour. Res.*, *45*(1), 1–5, doi:10.1029/2008WR007442.

450 Cardenas, M. B., and M. S. Markowski (2011), Geoelectrical imaging of hyporheic
451 exchange and mixing of river water and groundwater in a large regulated river,
452 *Environ. Sci. Technol.*, *45*(4), 1407–1411, doi:10.1021/es103438a.

453 Cardenas, M. B., J. L. Wilson, and V. a. Zlotnik (2004), Impact of heterogeneity, bed
454 forms, and stream curvature on subchannel hyporheic exchange, *Water Resour. Res.*,
455 *40*(8), n/a--n/a, doi:10.1029/2004WR003008.

456 Coleman, A. M., K. B. Larson, D. L. Ward, and J. W. Lettrick, (2010), Development of a
457 High-Resolution Bathymetry Dataset for the Columbia River through the Hanford
458 Reach, *Rep. PNNL-19878*, Pacific Northwest National Laboratory, Richland,
459 Washington.

460 Conant, B. (2004), Delineating and Quantifying Ground Water Discharge Zones Using
461 Streambed Temperatures, *Ground Water*, *42*(2), 243–257, doi:10.1111/j.1745-
462 6584.2004.tb02671.x.

463 Crispell, J. K., and T. A. Endreny (2009), Hyporheic exchange flow around constructed
464 in-channel structures and implications for restoration design, *Hydrol. Process.*,
465 *1168*(January), 1158–1168, doi:10.1002/hyp.

466 Findlay, S., D. Strayer, C. Goumbala, and K. Gould (1993), Metabolism of streamwater
467 dissolved organic carbon in the shallow hyporheic zone, *Limnol. Oceanogr.*, *38*(7),
468 1493–1499, doi:10.4319/lo.1993.38.7.1493.

469 Freeze, R. A., and J. A. Cherry, (1979), *Groundwater*, Prentice Hall Inc., Upper Saddle
470 River, N. J.

471 Fritz, B. G., and E. V. Arntzen (2007), Effect of rapidly changing river stage on uranium
472 flux through the hyporheic zone, *Ground Water*, *45*(6), 753–760, doi:10.1111/j.1745-
473 6584.2007.00365.x.

474 Fritz, B. G., R. D. Mackley, N.P. Kohn, G.W. Patton, T. J. Gilmore, D. P. Mendoza, D.
475 McFarland, A. L. Bunn, and E. V. Arntzen, (2007), Investigation of the Hyporheic
476 Zone at the 300 Area, Hanford Site, *Rep. PNNL-16805*, Pacific Northwest National
477 Laboratory, Richland, Washington.

478 Gerecht, K. E., M. B. Cardenas, A. J. Guswa, A. H. Sawyer, J. D. Nowinski, and T. E.
479 Swanson (2011), Dynamics of hyporheic flow and heat transport across a bed-to-
480 bank continuum in a large regulated river, *Water Resour. Res.*, *47*(3), 1–12,
481 doi:10.1029/2010WR009794.

482 Gomez-velez, J. D., and J. W. Harvey (2014), A hydrogeomorphic river network model
483 predicts where and why hyporheic exchange is important in large basins, *Geophys.*
484 *Res. Lett.*, 1–10, doi:10.1002/2014GL061099.Received.

485 Gomez-Velez, J. D., J. W. Harvey, M. B. Cardenas, and B. Kiel (2015), Denitrification in
486 the Mississippi River network controlled by flow through river bedforms, *Nat.*
487 *Geosci.*, *8*(October), 1–8, doi:10.1038/ngeo2567.

488 Gooseff, M. N. (2010), Defining Hyporheic Zones - Advancing Our Conceptual and
489 Operational Definitions of Where Stream Water and Groundwater Meet, *Geogr.*
490 *Compass*, *4*(8), 945–955, doi:10.1111/j.1749-8198.2010.00364.x.

Hartman, M. J. and P. E. Dresel (1998), Hanford Site Groundwater Monitoring for Fiscal Year 1997, *Rep. PNNL-11793*. Pacific Northwest National Laboratory, Richland, Washington.

Harvey, J., and M. Gooseff (2015), River corridor science: Hydrologic exchange and ecological consequences from bedforms to basins, *Water Resour. Res.*, *51*(9), 6893–6922, doi:10.1002/2015WR017617.

Harvey, J. W., and B. J. Wagner (2000), Quantifying hydrologic interactions between streams and their subsurface hyporheic zones, in *Streams and Ground Waters*, edited by J. B. Jones and P. J. Mulholland, pp. 3–44, Elsevier, New York, N. Y.

Harvey, J. W., B. J. Wagner, and K. E. Bencala (1996), Evaluating the reliability of the stream tracer approach to characterize stream-subsurface water exchange, *Water Resour. Res.*, *32*(8), 2441–2451, doi:10.1029/96WR01268.

Hou Z., W.C. Nelson, J. C. Stegen, C. J. Murray, E. Arntzen, C. Murray, A. R. Crump, D. W. Kennedy, T. D. Scheibe, J. K. Fredrickson, and J. M. Zachara (2016, in review) Geochemical and Microbial Community Attributes in Relation to Hyporheic Zone Geological Facies. *Scientific Reports*.

Janssen, F., M. B. Cardenas, A. H. Sawyer, T. Dammrich, J. Krietsch, and D. De Beer (2012), A comparative experimental and multiphysics computational fluid dynamics study of coupled surface-subsurface flow in bed forms, *Water Resour. Res.*, *48*(8), 1–16, doi:10.1029/2012WR011982.

Kalbus, E., F. Reinstorf, and M. Schirmer (2006), Measuring methods for groundwater, surface water and their interactions: a review, *Hydrol. Earth Syst. Sci. Discuss.*, *3*(4), 1809–1850, doi:10.5194/hessd-3-1809-2006.

Kiel, B. a., and M. Bayani Cardenas (2014), Lateral hyporheic exchange throughout the

515 Mississippi River network, *Nat. Geosci.*, *7*(May), 413–417, doi:10.1038/ngeo2157.

516 Lautz, L. K., and D. I. Siegel (2006), Modeling surface and ground water mixing in the
517 hyporheic zone using MODFLOW and MT3D, *Adv. Water Resour.*, *29*(11), 1618–
518 1633, doi:10.1016/j.advwatres.2005.12.003.

519 Morrice, J. A., H. M. Valett, C. N. Dahm, and M. E. Campana (1997), Alluvial
520 characteristics, groundwater-surface water exchange and hydrological retention in
521 headwater streams, *Hydrol. Process.*, *11*(March 1995), 253–267,
522 doi:10.1002/(SICI)1099-1085(19970315)11:3<253::AID-HYP439>3.0.CO;2-J.

523 Niehus, S. E., W. A. Perkins, M. C. Richmond (2014), Simulation of Columbia River
524 Hydrodynamics and Water Temperature from 1917 through 2011 in the Hanford
525 Reach, *Rep. PNWD-3278* (p. 148). Battelle-Pacific Northwest Division, Richland,
526 Washington, doi: 10.13140/RG.2.1.5146.8409.

527 Poff, N. L., J. D. Allan, M. B. Bain, J. R. Karr, K. L. Prestegaard, B. D. Richter, R. E.
528 Sparks, and J. C. Stromberg (1997), The Natural Flow Regime: A paradigm for river
529 conservation and restoration N., *Bioscience*, *47*(11), 769–784, doi:10.2307/1313099.

530 Poston, T.M., R.W. Hanf, R.L. Dirkes, and L.F. Morasch (2006), Hanford Site
531 Environmental Report for Calendar Year 2005, *Rep. PNNL-15892*, Pacific Northwest
532 National Laboratory, Richland, Washington.

533 Sawyer, A., M. Bayani Cardenas, A. Bomar, and M. Mackey (2009), Impact of dam
534 operations on hyporheic exchange in the riparian zone of a regulated river, *Hydrol.*
535 *Process.*, *23*(15), 2129–2137, doi:10.1002/hyp.7324.

536 Slater, L. D., D. Ntarlagiannis, F. D. Day-Lewis, K. Mwakanyamale, R. J. Versteeg, A.
537 Ward, C. Strickland, C. D. Johnson, and J. W. Lane (2010), Use of electrical imaging
538 and distributed temperature sensing methods to characterize surface water-

groundwater exchange regulating uranium transport at the Hanford 300 Area, Washington, *Water Resour. Res.*, *46*(10), 1–13, doi:10.1029/2010WR009110.

Sobczak, W. V., and S. Findlay (2002), Variation in bioavailability of dissolved organic carbon among stream hyporheic flowpaths, *Ecology*, *83*(11), 3194–3209, doi:10.2307/3071853.

Stonedahl, S. H., J. W. Harvey, A. Wörman, M. Salehin, and A. I. Packman (2010), A multiscale model for integrating hyporheic exchange from ripples to meanders, *Water Resour. Res.*, *46*(12), n/a--n/a, doi:10.1029/2009WR008865.

Todd, D. K. and Mays, L. W. (2005), *Groundwater Hydrology*, Wiley, Hoboken, N. J.

Tonina, D., and J. M. Buffington (2007), Hyporheic exchange in gravel bed rivers with pool-riffle morphology: Laboratory experiments and three-dimensional modeling, *Water Resour. Res.*, *43*(1), n/a--n/a, doi:10.1029/2005WR004328.

Trauth, N., C. Schmidt, U. Maier, M. Vieweg, and J. H. Fleckenstein (2013), Coupled 3-D stream flow and hyporheic flow model under varying stream and ambient groundwater flow conditions in a pool-riffle system, *Water Resour. Res.*, *49*(9), 5834–5850, doi:10.1002/wrcr.20442.

Turcotte, D.L., Schubert, G. (1982), *Geodynamics: Applications of Continuum Physics to Geological Problems*, John Wiley & Sons, New York, N. Y.

Valett, H. M., J. a. Morrice, C. N. Dahm, and M. E. Campana (1996), Parent lithology, surface-groundwater exchange, and nitrate retention in headwater streams, *Limnol. Oceanogr.*, *41*(2), 333–345, doi:10.4319/lo.1996.41.2.0333.

Vandersteen, G., U. Schneidewind, C. Anibas, C. Schmidt, P. Seuntjens, and O. Batelaan (2015), Determining groundwater-surface water exchange from temperature-time series: Combining a local polynomial method with amaximum likelihood

563 estimator, *Water Resour. Res.*, *51*, 922–939, doi:10.1002/2014WR015829.

564 Williams M.D., P.D. Thorne, M.L. Rockhold, Y. Chen (2008), Three-Dimensional
565 Groundwater Models of the 300 Area at the Hanford Site, Washington State, *Rep.*
566 *PNNL-17708*. Pacific Northwest National Laboratory, Richland, Washington.

567 Winter, T. C. (1999), Relation of streams, lakes, and wetlands to groundwater flow
568 systems, *Hydrogeol. J.*, *7*(1), 28–45, doi:10.1007/s100400050178.

569 Zarnetske, J. P., R. Haggerty, S. M. Wondzell, and M. A. Baker (2011a), Dynamics of
570 nitrate production and removal as a function of residence time in the hyporheic
571 zone, *J. Geophys. Res. Biogeosciences*, *116*(1), 1–12, doi:10.1029/2010JG001356.

572 Zarnetske, J. P., R. Haggerty, S. M. Wondzell, and M. A. Baker (2011b), Labile dissolved
573 organic carbon supply limits hyporheic denitrification, *J. Geophys. Res.*
574 *Biogeosciences*, *116*(4), doi:10.1029/2011JG001730.

575 Zhou, T., and T. A. Endreny (2013), Reshaping of the hyporheic zone beneath river
576 restoration structures: Flume and hydrodynamic experiments, *Water Resour. Res.*,
577 *49*(8), 5009–5020, doi:10.1002/wrcr.20384.

578 Zhou, T., M. Huang, J. Bao, Z. Hou, E. Arntzen, R. Mackley, A. Crump, A. Goldman, X.
579 Song, Y. Xu, C. Murray, J. Stegen, and J. Zachara (2017, submitted), Spatial and
580 temporal variations of shallow water hyporheic exchange in a regulated large river
581 reach, *Groundwater*.

582

583

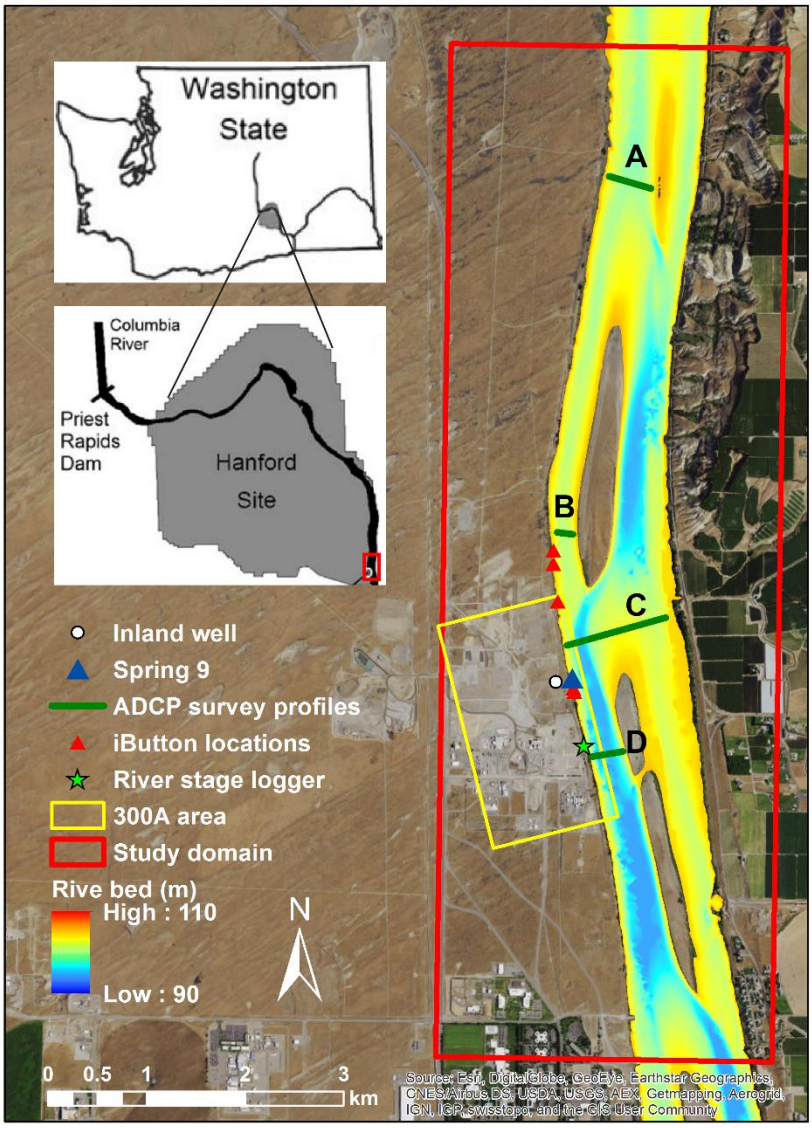

584

585 Figure 1 Study site

586

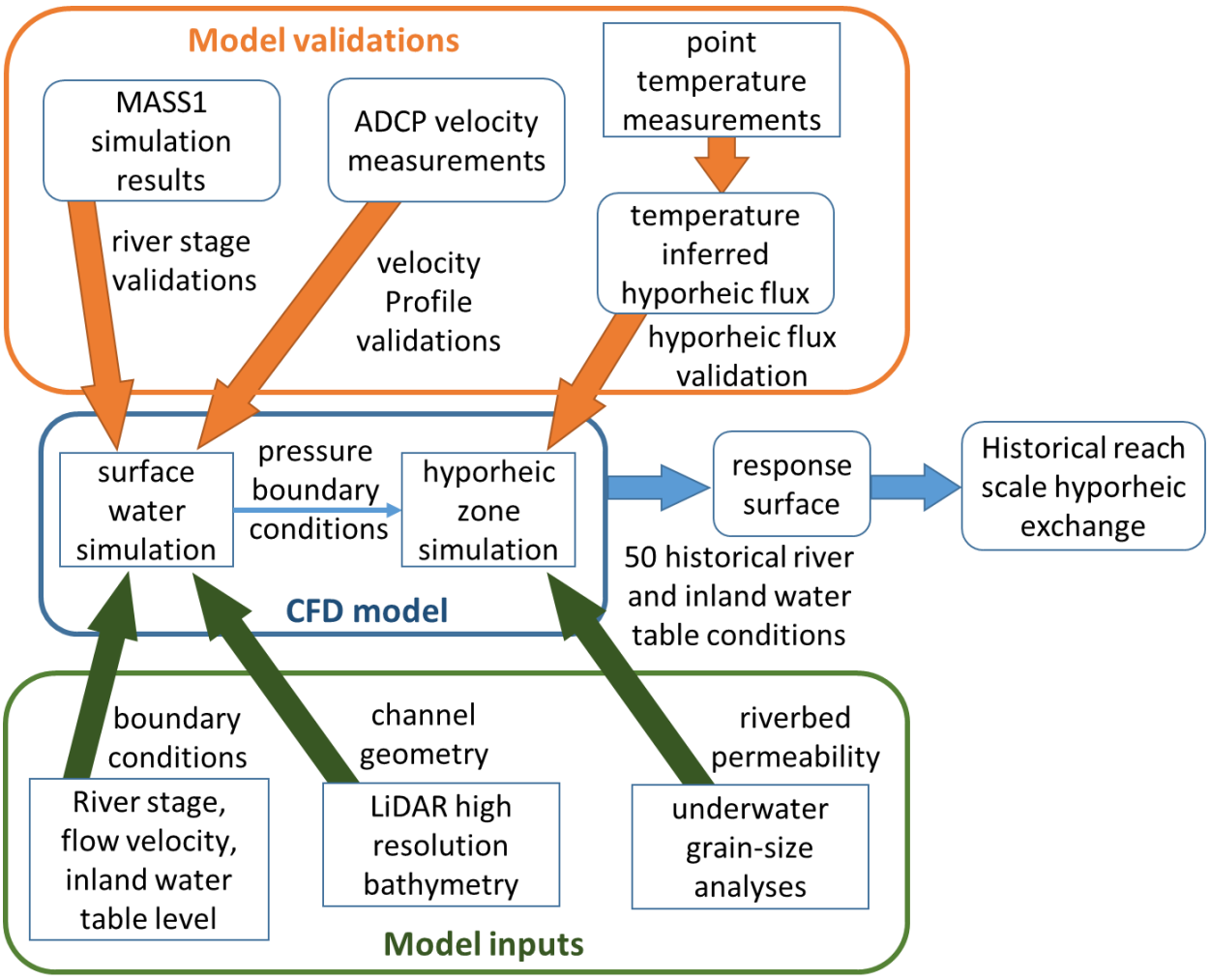

587

588 Figure 2 Diagram of the work flow for model configuration

589 and validation

590

591

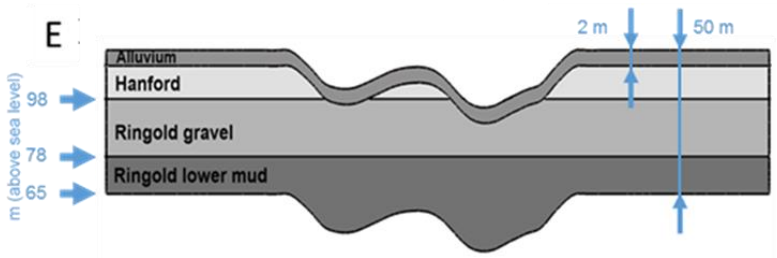

592 Figure 3 Subsurface configuration in the CFD model

593 (transect C in Figure 1)

594

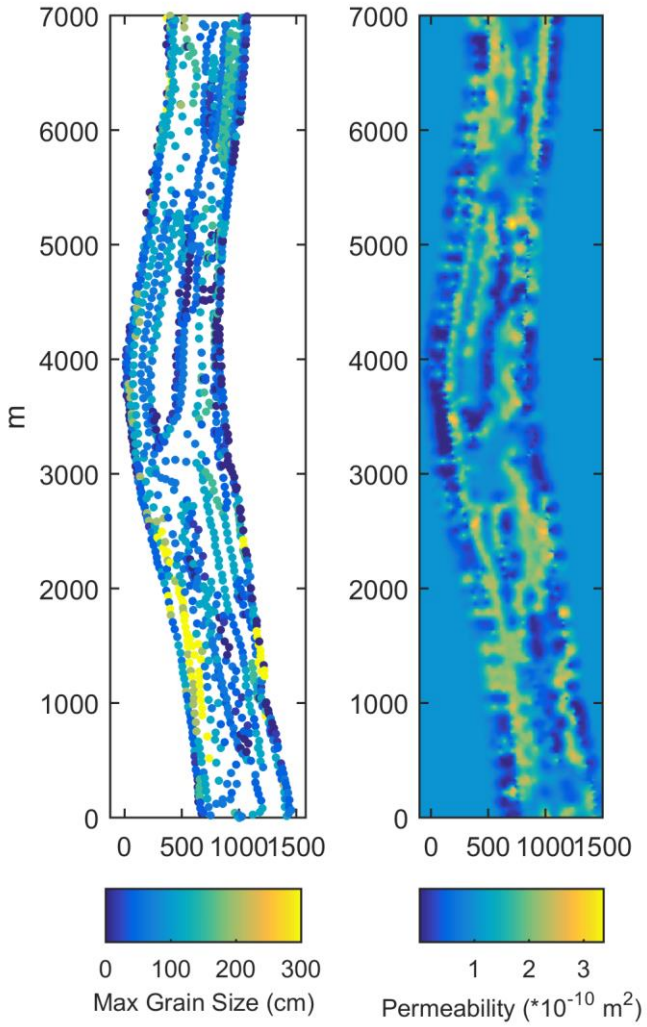

595

596 Figure 4 Permeability of the alluvium layer (right panel)
597 estimated from the maximum grain size generated from
598 underwater video footage (left panel).

599

600

601

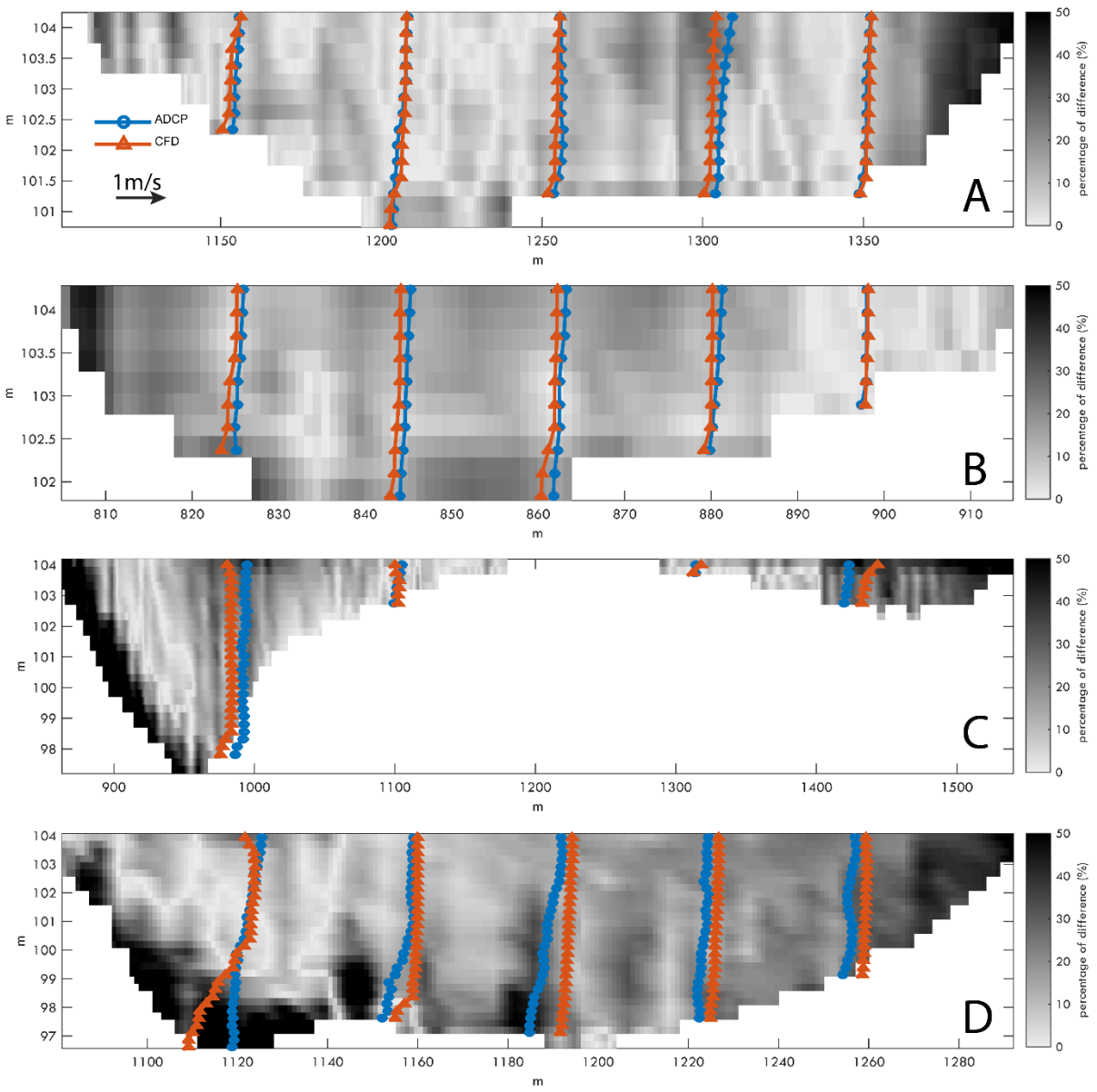

602

603 **Figure 5:** Comparison between CFD simulated streamwise
604 velocity (v_y) profiles with ADCP measurements at Cross Sections
605 A to D as marked in Figure 1. Color-coded lines are v_y vs. depth
606 profiles at 1/6, 1/3, 1/2, 2/3, and 5/6 width of the cross sections.
607 Grey scale contour maps show the percentage of differences
608 between ADCP measurements and CFD predictions.
609

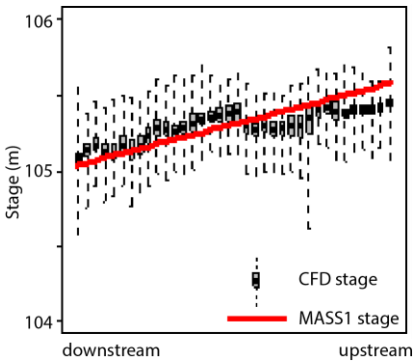

610

611 Figure 6 Comparison between CFD-simulated river stages

612 with those from MASS1

613

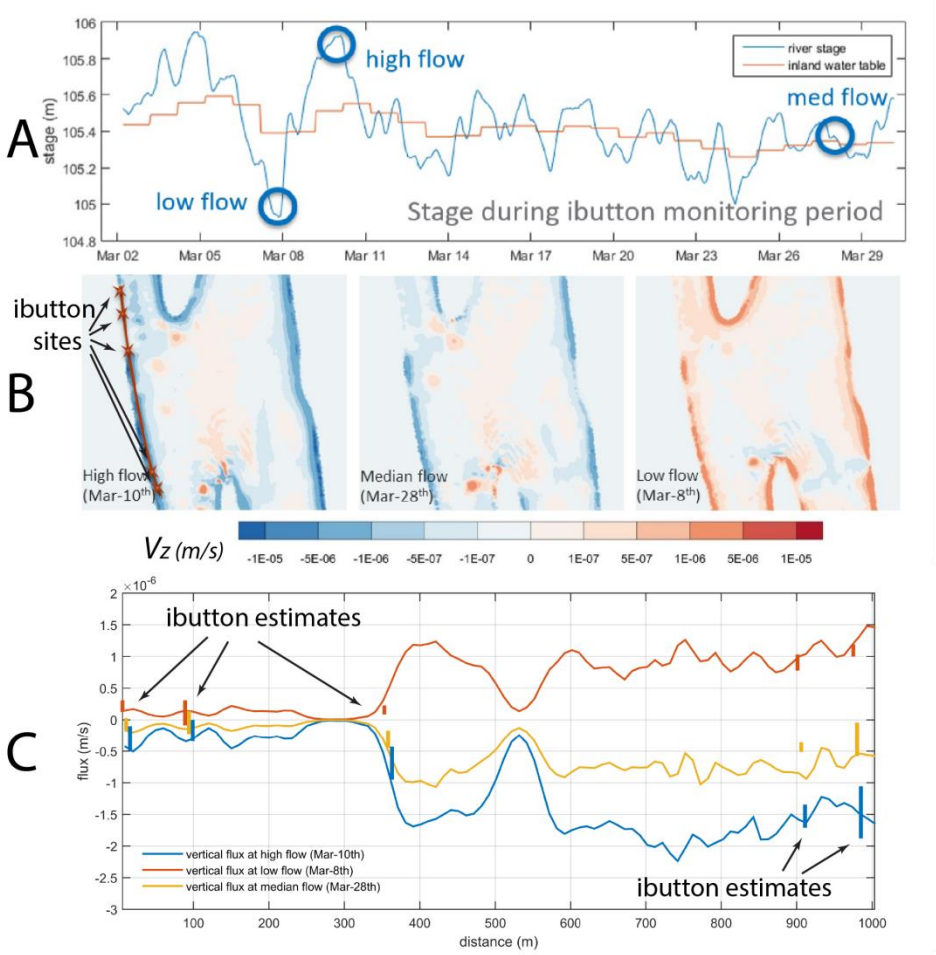

614

615 **Figure 7:** Comparison of hyporheic fluxes on the river bed
616 between the CFD simulations and iButton measurements. A:
617 Flow conditions and inland water stages during the iButton
618 measurement period; B: CFD simulated hyporheic fluxes on the
619 river bed for the low, median, and high flow conditions; C:
620 Comparison of hyporheic fluxes along the shoreline between the
621 CFD simulations and iButton measurements.

622

623

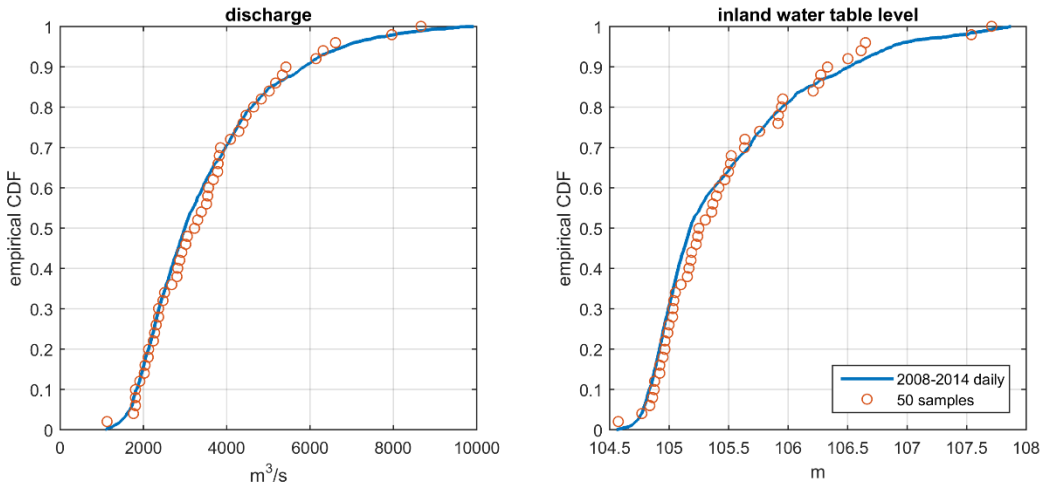

624

625 Figure 8 Comparison of empirical CDFs of discharges (left
626 panel) and inland water table levels (right panel) derived based
627 on all historical daily records over the period of 2008 to 2014 with
628 the 50 selected flow conditions used as the CFD simulation
629 inputs.

630

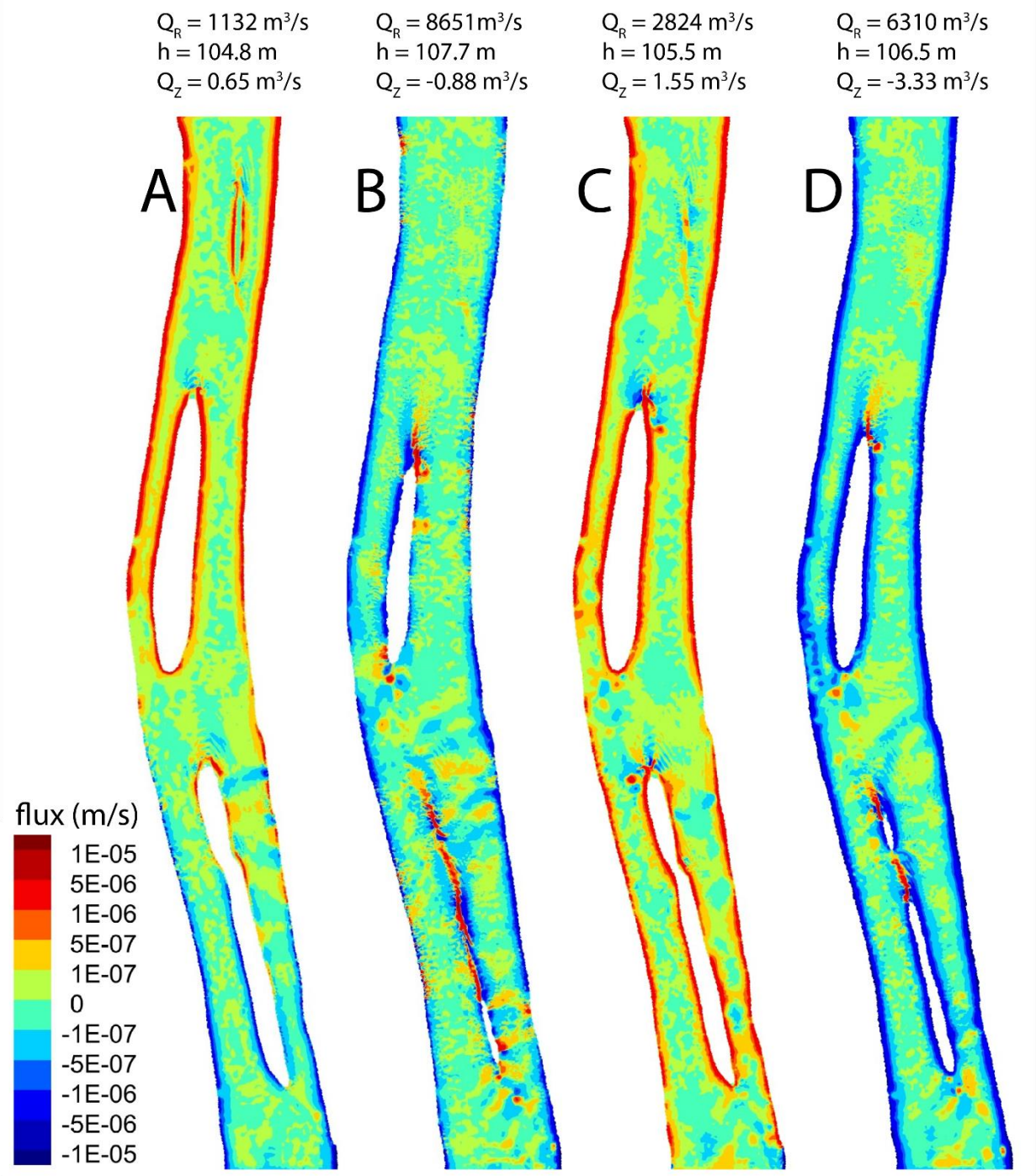
Q_R = 1132 m³/s
h = 104.8 m
Q_Z = 0.65 m³/s
Q_R = 8651m³/s
h = 107.7 m
Q_Z = -0.88 m³/s
Q_R = 2824 m³/s
h = 105.5 m
Q_Z = 1.55 m³/s
Q_R = 6310 m³/s
h = 106.5 m
Q_Z = -3.33 m³/s
A
B
C
D
flux (m/s)
1E-05
5E-06
1E-06
5E-07
1E-07
0
-1E-07
-5E-07
-1E-06
-5E-06
-1E-05

631

632 Figure 9 Spatial distribution of vertical fluxes over the
633 modeling domain at the lowest river discharge (A), highest river
634 discharge (B), as well as strongest hyporheic zone discharging
635 condition (C) and strongest recharging condition (D).

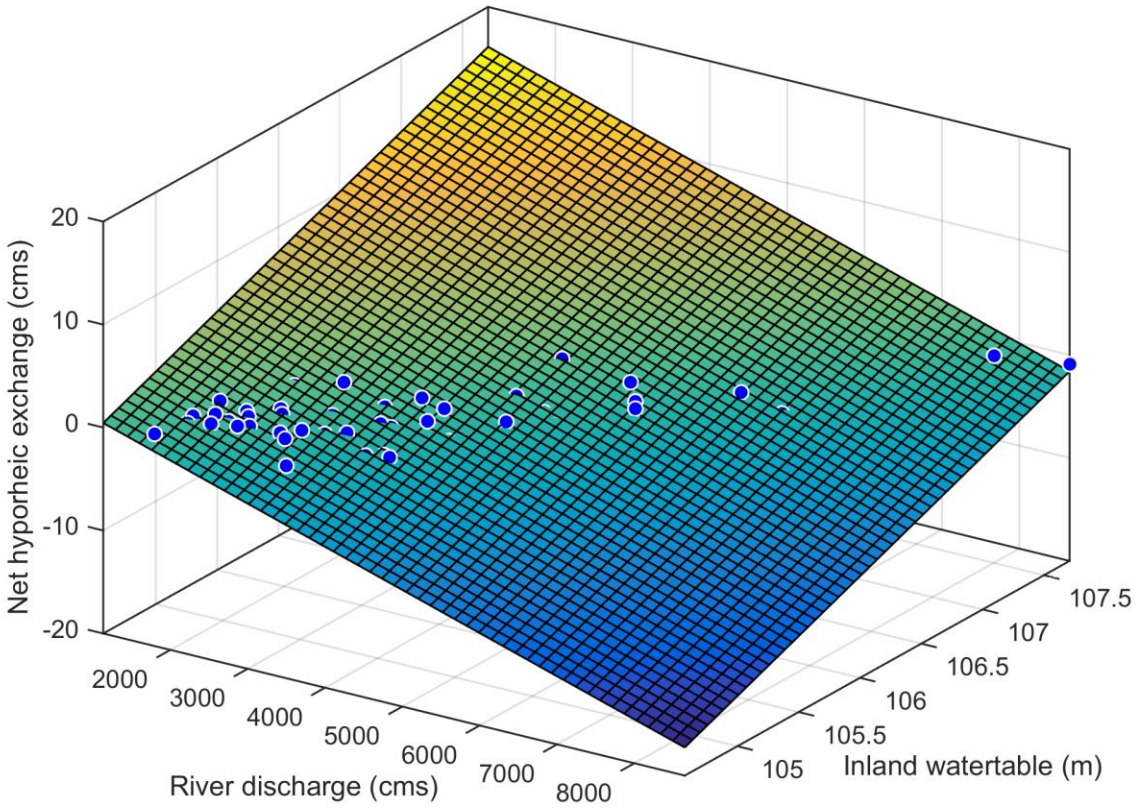

Figure 10 Fitted surface of the net vertical hyporheic discharge over the riverbed of the entire study domain as a function of river discharge and inland water table level at the monitoring well based on the CFD simulations.

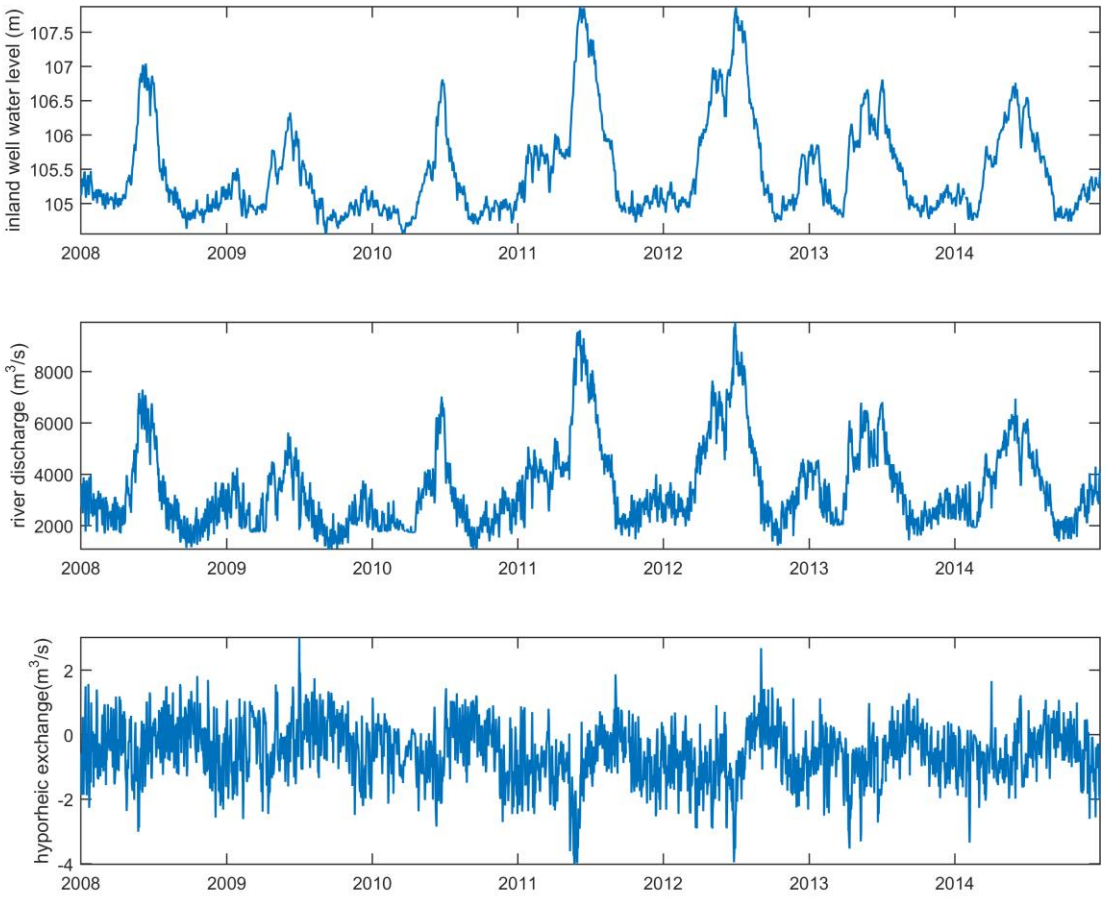

Figure 11 Historical inland water level (A), river discharge (B) and estimated vertical discharge of the study reach (C) from 2008 to 2014

652

653 Table 1 Physical parameters used in the simulations

Parameters	Aquifer unit			
	Alluvium layer	Hanford	Ringold gravel	Ringold lower mud
Porosity	0.18	0.373	0.294	0.351
Horizontal permeability (m^2)	estimated from grain size	1.23×10^{-8}	1.93×10^{-9}	2.53×10^{-15}
Vertical permeability (m^2)	estimated from grain size	1.23×10^{-9}	6.76×10^{-10}	6.8×10^{-16}

654

655

656

Supplementary Materials for

Quantifying hyporheic exchange dynamics in a highly regulated large river reach

Zhou T.[1], J. Bao[1], M. Huang[1], Z. Hou[1], E. Arntzen[1], S. Harding[1], S. Titzler[1], C. Murray[1], W. Perkins[1], X. Chen[1], J. Stegen[1], G. Hammond[2], P. Thorne[1], J. Zachara[1]

3. Pacific Northwest National Laboratory, Richland, WA, USA
4. Sandia National Laboratory, Albuquerque, NM, USA

S.1 the Computational Fluid Dynamic (CFD) Model

STAR-CCM+ CFD software [*CD-adapco*, 2015] was used for 3-dimensional surface and subsurface flow simulations. The numerical model involves solving the mass and momentum conservation equations for fluid dynamics. The mass conservation equation is

$$\frac{\partial \rho}{\partial t} + \nabla \cdot (\rho \vec{v}) = 0, \quad (1)$$

where ρ is fluid density, $\vec{v}$ is velocity vector, and t is time. With the Boussinesq hypothesis [*Schmitt*, 2007], the RANS [*O.Reynolds*, 1895] momentum equation is in the form of

$$\frac{\partial (\rho \vec{v})}{\partial t} + \nabla \cdot (\rho \vec{v} \vec{v}) = -\nabla p - \nabla \cdot [\mu (\nabla \vec{v} + \nabla \vec{v}^T)] + \rho \vec{g}, \quad (2)$$

where p is pressure, $\vec{g}$ is gravity acceleration, and μ is effective viscosity, which can be calculated as

$$\mu = \mu_m + \mu_t. \quad (3)$$

μ_m is molecular dynamic viscosity, and μ_t is turbulent viscosity. In this study, for acquiring the flexibility on the mesh, realizable $k - \varepsilon$ two-layer turbulence model and two-layer all y^+ wall treatment are used [*Versteeg and Malaasekera*, 1995; *Liu et al.*, 2012; CD-adapco, 2015]. Therefore μ_t is calculated by a blending function as follows:

$$\mu_t = \lambda \mu_t|_{k-\varepsilon} + (1 - \lambda) \mu_t|_{two-layer}. \quad (4)$$

$\mu_t|_{k-\varepsilon}$ is turbulent viscosity derived from the realizable $k - \varepsilon$ model (Shih *et al.*, 1995), and $\mu_t|_{two-layer}$ is turbulent viscosity derived from a two-layer formulation through the Wolfstein model [*Wolfstein*, 1969]. λ is a blending factor, which is a function of Reynolds number depending on the wall distance [*Jongen*, 1998]. The VOF model is applied for simulating and tracking the water-air interface:

$$\frac{\partial \alpha_w}{\partial t} + \nabla \cdot (\vec{v} \alpha_w) = 0, \quad (5)$$

where α_w is the water volume fraction. The fluid density ρ and molecular dynamic viscosity μ_m become

$$\rho = \alpha_w \rho_w + (1 - \alpha_w)\rho_a \,, \tag{6}$$

$$\mu_m = \alpha_w \mu_{mw} + (1 - \alpha_w)\mu_{ma} \,, \tag{7}$$

where ρ_w is water density, ρ_a is air density, μ_{mw} is water molecular dynamic viscosity, and μ_{ma} is air molecular dynamic viscosity.

In the subsurface domain, because the magnitude of velocities is very small, by adding a large viscous resistance term for subsurface porous media, the momentum equation (2) is simplified to [*Huang and Ayoub*, 2006]

$$\nabla p = -\bar{\bar{R}}_v \vec{v} \tag{8}$$

$\bar{\bar{R}}_v$ is the viscous porous resistance tensor. For the subsurface domain, it can be assumed as

$$\bar{\bar{R}}_v = \begin{bmatrix} \frac{\mu_m}{k_H} & 0 & 0 \\ 0 & \frac{\mu_m}{k_H} & 0 \\ 0 & 0 & \frac{\mu_m}{k_V} \end{bmatrix} \tag{9}$$

k_H and k_V are the horizontal and vertical permeability respectively.

The simulation domain is divided into two sub-domains: the surface flow region and the subsurface flow region, which share the river bed surface as the interface. For a given set of boundary conditions, including the upstream river stage, averaged upstream river water velocities, the downstream river stage, the model spins up surface water dynamics to an equilibrium state by assuming the riverbed as a non-penetrable wall. The pressure field at the river bed surface (**Figure S1**) and VOF field are then

710 extracted from the surface flow region and applied to the subsurface flow domain as the
711 upper boundary condition. By applying the pressure and VOF boundary conditions on
712 the river bed, the velocity, pressure, and VOF in the subsurface flow region can be
713 solved by Eqs. (1), (5) and (8). Meanwhile, flow velocities across the river bed can be
714 solved as well in the subsurface region, and an instantaneous map of simulated
715 hyporheic fluxes on the river bed is shown in the subsurface flow region in **Figure S1**.
716 This coupling strategy is therefore a one-way coupling approach because fluxes on the
717 river bed are not fed back into the surface flow region to inform its simulation. There
718 are two main reasons to using the one-way coupling. Firstly, the magnitude of the
719 hyporheic flux ($\sim 1 \times 10^{-6}\ m/s$) is negligible, compared to the velocity of surface water
720 ($\sim 1\ m/s$) in the river channel . Secondly, the turbulent flow velocity profile near the
721 river bed in the surface flow region is derived from the turbulence wall function
722 [*Versteeg and Malaasekera*, 1995; *Liu et al.*, 2012; *CD-adapco*, 2015] instead of using the
723 simple Dirichlet boundary condition at the river bed. However, the available wall
724 functions cannot handle the situation that flux penetrates the boundary wall.

725 S.2 MASS1 model

726 The Modular Aquatic Simulation System in one-Dimension (MASS1) model was
727 developed at the Pacific Northwest National Laboratory. and has been applied to a
728 variety of problems in the Columbia River basin. *Richmond et al.* [2002] applied MASS1
729 to analyze several dissolved gas reduction strategies for Columbia and Snake River
730 dams; *Richmond and Perkins* [2002] used MASS1 to simulate temperature in the lower
731 Snake River; *McMichael et al*. [2005] estimated dewatering time histories at a salmon
732 spawning location using MASS1; and MASS1 was used by *Tiffan et al.* [2002] to supply
733 stage and discharge boundary conditions to a two-dimensional model of the Hanford
734 Reach. MASS1 simulates steady and unsteady flow in rivers and canals by solving the
735 one-dimensional, cross-section averaged equations of mass and momentum

736 conservations (St. Venant equations). The friction slope used in the momentum
737 equation was derived based on Manning's equation with the Manning's *n* values
738 ranging from 0.022 to 0.029 for the Hanford Reach. This range is consistent with
739 measured values.

740 Calendar years 1998-2000 were used to validate the MASS1 model simulation
741 results. In each simulated year, there was a strong linear relationship between
742 simulated and observed stage. The R^2 values between the stages were greater than 0.9
743 during the validation period with average bias about ±0.03m. Generally,MASS1
744 simulated hourly stage with an MAE of less than 0.15m and with a bias of less than 0.06
745 m, indicating that the MASS1 results were very close to the observations at the hourly
746 basis.

747

748 CD-ADAPCO (2015).STAR-CCM+ user guide, version 10.04

749 Huang H and Ayoub J. (2006), Applicability of the Forchheimer Equation for Non-
750 Darcy Flow in Porous Media. *SPE Journal*, 112-122.

751 Jongen T. (1998), Simulation and Modeling of Turbulent Incompressible Flows. École
752 polytechnique fédérale de Lausanne.

753 Liu CC, Ferng YM, Shih CK. (2012) CFD evaluation of turbulence models for flow
754 simulation of the fuel rod bundle with a spacer assembly. *Applied Thermal*
755 *Engiineering*, 40: 389-396.

756 McMichael, G.A., Rakowski, C.L., James, B.B., Lukas, J.A., (2005), Estimated fall chinook
757 salmon survival to emergence in dewatered redds in a shallow side channel of the
758 Columbia River. *North American Journal of Fisheries Management* 25 (3), 876–884

759 Reynolds O. (1895) On the Dynamical Theory of Incompressible Viscous Fluids and the
760 Determination of the Criterion. *Philosophical Transactions of the Royal Society of*
761 *London*, 186: 123-164.

762 Richmond, M.C., Perkins, W.A., (2002), Regional scale simulation of water temperature
763 variations in the Columbia River basin. *Research and Extension Regional Water*
764 *Quality Conference Program and Proceedings*. Washington State University, Pullman,
765 Washington, Vancouver, Washington

766 Richmond, M.C., Perkins, W.A., Chien, Y. (2002), Regional scale simulation of water
767 temperature and dissolved gas variations in the Columbia River basin. In:
768 *HydroVision 2002 Technical Papers*. HCI Publications, Kansas City, Missouri,
769 Portland, Oregon

770 Schmitt FG. (2007). About Boussinesq's turbulent viscosity hypothesis: historical
771 remarks and a direct evaluation of its validity. *Comptes Rendus Mécanique*, 335: 617-
772 627.

773 Tiffan, K.F., Garland, R.D., Rondorf, D.W., (2002), Quantifying flow-dependent changes
774 in subyearling fall chinook salmon rearing habitat using two-dimensional spatially
775 explicit modeling. *North American Journal of Fisheries Management* 22 (3), 713–726.

776 Versteeg HK and Malaasekera W. (1995) *An introduction to computational fluid dynamics:*
777 *the finite volume method*. Wiley.

778 Wolfstein M. (1969), The velocity and temperature distribution in one-dimensional flow
779 with turbulence augmentation and pressure gradient. *International Journal of Heat*
780 *and Mass Transfer*, 12: 301-318.

781

782

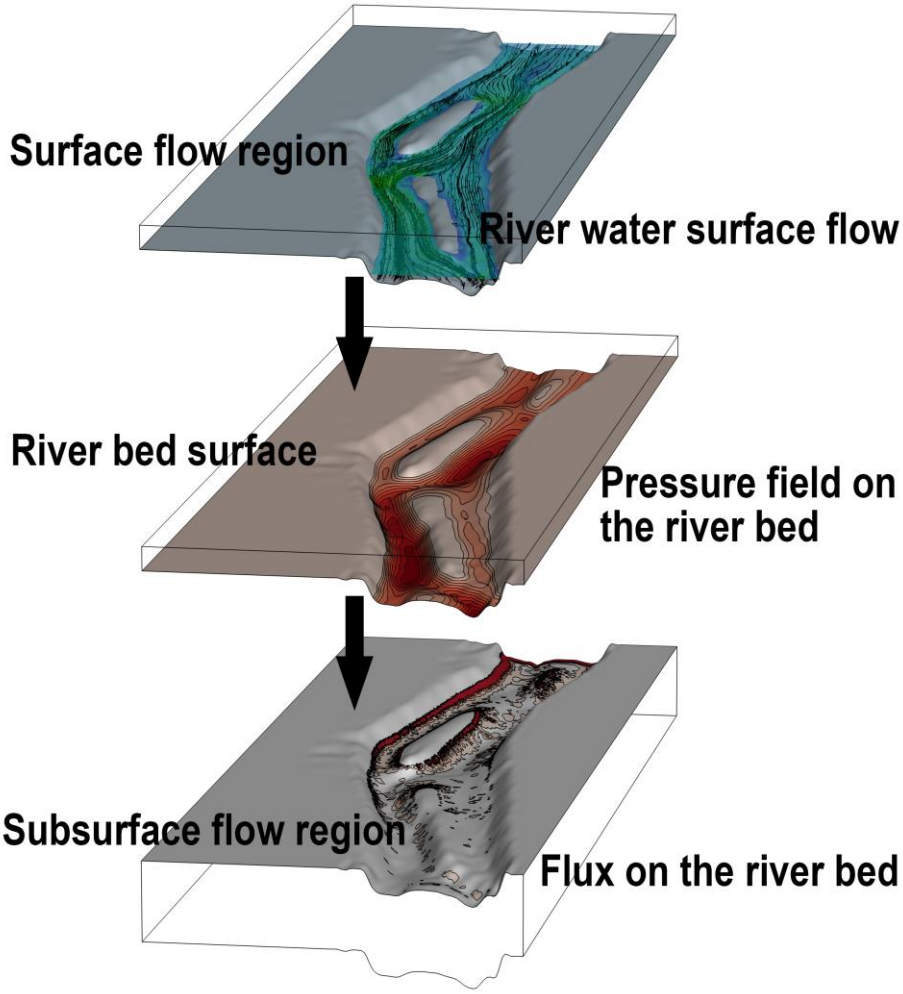

783

784 Figure S1 CFD model surface-subsurface coupling configuration

785